Journal of Biomechanics, Volume 49, Issue 14, Issue October, 2016, Pages 3444-3451
DOI: 0.1016/j.jbiomech.2016.09.016

Impact of P2RX7 ablation on the morphological, mechanical and tissue properties of bones in a murine model of Duchenne Muscular Dystrophy

N.S. Mohamad[1], A. Sinadinos[2], D. C. Górecki[2], P. Zioupos[3], J. Tong[1]*
[1] *Mechanical Behaviour of Materials Group, School of Engineering, University of Portsmouth, UK*
[2] *School of Pharmacy and Biomedical Sciences, University of Portsmouth, UK*
[3] *Biomechanics Labs, Cranfield Forensic Institute, Cranfield University, DA of the UK,*

** Corresponding author: Professor Jie Tong, School of Engineering, University of Portsmouth, Portsmouth PO1 3DJ, UK, +44 (0)23 9284 2326 (jie.tong@port.ac.uk)*

Abstract
Duchenne muscular dystrophy (DMD) is an inherited, lethal disorder characterised by progressive muscle degeneration and associated bone abnormalities. We have previously demonstrated that P2RX7 purinergic receptors contribute to the pathogenesis of DMD, and found that P2RX7 ablation alleviated the severity of the disease. In this work we have used a dystrophic *mdx* mouse crossed with the global P2RX7 receptor to generate a knockout mouse (*mdx*/P2X7$^{-/-}$), and compared its morphometric, mechanical and tissue properties against those of *mdx*, as well as the wild type (WT) and the P2RX7 knockout (P2X7$^{-/-}$). Micro-computed tomography (μCT), three-point bending testing, scanning electron microscopy (SEM) and nano-indentation were utilised in the study. The bones were analysed at approximately 4 weeks of age to examine the impact of P2RX7 ablation on the bone properties during the acute disease phase, before muscle wasting is fully developed. The results show that P2RX7 purinoceptor ablation has produced improvement or significant improvement in some of the morphological, the mechanical and the tissue properties of the dystrophic bones examined. Specifically, although the ablation produced smaller bones with significantly lower total cross-section area (Tt.Ar) and Second Moment of Area (SMA), significantly higher cortical bone area (Ct.Ar), cortical bone area ratio (Ct.Ar/Tt.Ar) and trabecular bone volume fraction (BV/TV) are found in the *mdx*/P2X7-/- mice than in any other types. Further, the *mdx*/P2X7$^{-/-}$ bones have relatively higher average flexural strength, work-to-fracture and significantly higher strain to failure compared with those of *mdx*, suggesting greater resistance to fracture. Indentation modulus, elasticity and creep are also significantly improved in the knockout cortical bones over those of *mdx*. These findings seem to suggest that specific pharmacological blockade of P2RX7 may improve dystrophic bones, with a potential for therapeutic application in the treatment of the disease.

Keywords: Bone μCT; animal models; DMD; P2XR7; morphometric properties; mechanical properties; mdx; bone modelling and remodelling; nano-indentation

INTRODUCTION

Duchenne muscular dystrophy (DMD) is the most common type of muscular dystrophy causing progressive muscle degeneration leading to severe disability and death of young men. DMD is also associated with cognitive impairment. Both patients (Rufo et al., 2011) and *mdx* (DMD model) mice (Nakagaki et al., 2011) were found to have lower bone mass, which is strongly associated with the degree of motor function and muscle strength.

The ability of bone to adapt to mechanical loads is usually linked to muscle activity, and bone loss in muscle paralysis is indicative of the importance of mechanical stimulation for bone regulation. In the late stages of DMD progression, the impact of muscle loss on the dystrophic bone structure is evident. However, early bone abnormalities found prior to substantial muscle loss indicate that there may be other factors inherent to DMD, which also contribute to the loss of bone mass (Anderson et al., 1993; Bianchi and Morandi, 2008; Nakagaki and Camilli, 2012). Studies by Anderson et al. (1993), Rufo et al. (2011) and Novotny et al. (2011) showed up to 50% loss in strength and stiffness in *mdx* mouse model of DMD compared to those of the control, resulting in the development of micro-damage (Saito and Marumo, 2010) and bone fracture (Bianchi and Morandi, 2008).

Several scenarios have been envisaged on the mechanisms behind the DMD bone abnormality (Abou-Khalil et al., 2013; Bianchi et al., 2003; Rufo et al., 2011). DMD causes absence of dystrophin, which disrupts structural scaffolds involving dystrophin-associated proteins and loss of anchoring for specific signalling proteins (Blake et al., 2002). Therefore, the absence of dystrophin could be directly responsible for bone structure alterations. However, there is no data on dystrophin being expressed in osteoblasts or

Journal of Biomechanics, Volume 49, Issue 14, Issue October, 2016, Pages 3444-3451
DOI: 0.1016/j.jbiomech.2016.09.016

osteoclasts. On the other hand, dystrophic muscle degeneration is associated with chronic sterile inflammation. Abou-Khalil et al. (2013) demonstrated that chronic inflammation contributes to dystrophic bone damage. In DMD patients, prolonged corticosteroid treatment can further exacerbate this abnormality (Bianchi et al., 2003; Söderpalm et al., 2007).

DMD gene mutations are associated with P2RX7 purinoceptor up-regulation, which leads to the death of both human DMD (Ferrari et al., 1994) and *mdx* cells (Yeung et al., 2006; Young et al., 2012). P2RX7 activation in mdx muscles triggers a specific mechanism of autophagic cell death (Young et al., 2015). Recent work showed that this receptor is a good target for pharmacological treatment of DMD, as its genetic ablation (knockout) reduced both muscle loss and inflammation (Sinadinos et al., 2015). P2RX7 is expressed in both osteoblasts and osteoclasts, but it appears to have different roles in bone physiology and in disease states. If P2RX7 is abnormally active in dystrophic bones, its absence might improve the bone properties. On the other hand, activation of P2RX7 receptor has been linked primarily to osteoclast functions (Agrawal and Gartland, 2015; Gartland, 2012; Ke et al., 2003), hence its ablation could have a negative impact on the bone. We hypothesize that P2RX7 ablation would *not* exacerbate the dystrophic bone phenotype.

To test this hypothesis, we have used a previously established double mutant (mdx/P2X7-/-, Sinadinos et al., 2015), examined the morphometric, mechanical and tissue properties of long bones of *mdx*/P2X7$^{-/-}$ mice against those of *mdx* as well as wild type (WT) and P2RX7 knockout (P2X7$^{-/-}$) mice, using µCT imaging, three-point bending testing and nanoindentation.

MATERIALS AND METHODS

Animal models

The *mdx* mouse is considered the most appropriate pre-clinical model to test treatment efficacy for DMD (http://www.treat-nmd.eu/research/preclinical/dmd-sops/). All animal experiments were performed in accordance with the approvals of the Institutional Ethical Review Board and the Home Office UK (70/7479).

The *mdx*/P2X7$^{-/-}$ were generated by crossing P2RX7 receptor knockout male mice (Solle et al., 2001) with *mdx* C57Bl/10ScSn-Dmdmdx/J female mice (Harlan Lab, UK), and genotypes were confirmed by genomic DNA PCR (Sinadinos et al., 2015). Animals were maintained in a 12 hours light/dark cycle and fed normal diet and water ad libitum. The mouse bones were analysed at approximately 4 weeks of age, when the disease is fully manifested but the muscle loss and its effects on bone properties are thought not yet significant. A total of 24 male mouse bones were used in the study. These included wild-type (C57BL10, n=6), dystrophic (*mdx,* n=6) (Bulfield et al., 1984), P2X7$^{-/-}$ (n=6) (Solle et al., 2001) and *mdx*/P2X7$^{-/-}$ (n=6) (Young et al., 2015), as summarised in Table 1.

Sample Preparation

Tibias were dissected clean of muscles under a stereo-microscope, and placed in 10% buffered formalin overnight prior to saline storage at 4°C. The tibias were kept in the saline solution until they were ready for scanning and mechanical testing. Left tibias for each of the genotypes were used for µCT scanning after about 2 weeks in the saline solution, followed by three-point bending testing, SEM examination and nanoindentation in up to 50 weeks.

Micro-computed tomography (µCT)

The tibias were scanned using µCT X-Ray Inspection System (X-Tek Systems Ltd). The sample was fixed in a specimen holder and positioned vertically to allow a full 360° rotation. The holder was placed as close as possible to the detector to achieve high resolution. The x-ray settings for imaging were: V = 50-55kVp, I = 95-110µA and rotational step = 0.19°/360°. The voxel size was about 6-8µm^3.

A full data acquisition took approximately 90 minutes and the dataset was stored in VGI format prior to visualisation using VG Studio Max 2.0 (Volume Graphics, Germany). Further, CTPRO (Metris X-Tek, UK) was used to reduce noise and beam hardening artefacts. ImageJ (NIH, US) was used for image processing; whilst BoneJ (Doube et al., 2010) was used for image analysis and the determination of key bone parameters (Bouxsein et al., 2010). The determination of the threshold for bone segmentation was based on visual inspection and automatic thresholding (IsoData algorithm) (Bouxsein et al., 2010; Stock, 2009). The algorithm divides the image into object and background by taking an initial threshold, then the averages of the pixels at or below the threshold and pixels above are computed (Ridler and Calvard, 1978). The average of these two values was then computed, and the process was repeated until the threshold is larger than the composite average. The analyses were

Journal of Biomechanics, Volume 49, Issue 14, Issue October, 2016, Pages 3444-3451
DOI: 0.1016/j.jbiomech.2016.09.016

carried out in the regions of interest (ROI), as illustrated in Figure 1. A total of 100 contiguous µCT slices were taken 0.50 mm below the growth plate in the metaphyseal region of the proximal tibia, from which cortical and cancellous bones were separated manually to obtain the parameters for the trabecular bone; whilst 54 contiguous µCT slices were assessed 4.32 mm from the growth plate in the mid-tibia to characterise the cortical bone.

Three-point bending testing

The biomechanical properties of bones from each genotype were determined using a three-point bending arrangement (Vashishth, 2008). The bending jig has a V-shaped support to secure the distal and the proximal ends of the tibia during testing. The tibia was positioned horizontally with the anterior side upwards, and the load was applied downwards in the centre of the mid-tibia. The distance between the supports was 7 mm (Silva et al., 2004). The bones were loaded at a constant displacement rate of 0.155 mm/s until failure using a BOSE Testing Machine (ElectroForce® 3200). The load-displacement curves were obtained and used for the calculation of the structural and material properties, including peak load; flexural modulus, determined by the slope of the linear part of the load-displacement curve, and work-to-fracture, defined by the area under the load-displacement curve. The cross-sectional second moment of area (SMA) in the loading direction (anterior-posterior) was determined using the algorithm in BoneJ, where the two orthogonal axes, anterior-posterior and medial-lateral, intersect at the centroid. An average value of SMA was obtained from the values calculated from 20 slices taken in an area close to the load application. The stress and strain were obtained using Equations (1) and (2) (Jepsen et al., 2015; Turner, 2002):

$$\sigma = F\left(\frac{Lc}{4I}\right) \quad (1)$$

$$\varepsilon = d\left(\frac{12c}{L^2}\right) \quad (2)$$

where σ is the stress, F is the load, L is the length of the span, c is the distance from the centroid of the cross-section along the anterior-posterior axis to the edge of the cross-section in tension, I is the SMA, ε is the strain, and d is the displacement. The flexural strength and strain at failure were obtained from the stress-strain curves.

Scanning Electron Microscopy (SEM)

Following the three-point bending tests, the fracture surfaces of the failed distal tibias of each genotype were investigated using SEM to identify the possible mechanisms responsible for fracture. The tibias were coated with gold-palladium (Bozzola and Russel, 1999) and stored in a dust-free desiccator before scanning. The sample was placed horizontally in the SEM chamber (JSM-6060LV, JEOL, Japan) and the analyses were carried out at 15kV, with resolutions between 10 and 500 µm to enable the analysis at both macro and micro levels.

Nanoindentation

Nanoindentation was performed using a CSM-Nano Hardness Tester System (CSM Instruments SA; Switzerland; Indentation v.3.83), with a Berkovich-based pyramid diamond indenter, following the standard ISO 4577-1:2015. The bone preparation followed the procedures described in (Finnilä et al., 2010; Herlin et al., 2013; Zioupos and Rogers, 2006). Briefly the left tibias were cleaned, ultrasonicated and dried in a desiccator before being embedded in a low viscosity Kleer-Set resin (MetPrep, Conventry, UK). The specimens were then ground using silicon carbide papers and finally polished using 0.05 micron γ-alumina slurry (Zioupos and Rogers, 2006). For trabecular bones, the individual trabeculae were supported by injecting low viscosity superglue into the pores in the trabecular network unfilled by the Kleer-set resin. The average values of 8 indentations in cortical bone samples and 3 to 5 indentations in trabecular bone samples were taken in advanced (standard) and dynamic loading protocols. The indentation targets were carefully selected in the centre of the intended bone tissue using an optical microscope (Zhang et al., 2015).

For the advanced protocol, a trapezoidal loading waveform was applied with a loading/unloading rate of 20mN/min, plus a 30s hold at the maximum load 10mN. In the dynamic protocol, a sinusoidal waveform was used with a frequency of 1.0Hz and an amplitude of 1.0mN. The hardness and indentation modulus were measured following Oliver and Pharr (1992). The elastic modulus and Poisson's ratio of the diamond indenting were 1142 GPa and 0.07, respectively. The viscoelastic behaviour of the bones was analysed using the dynamic protocol (Finnilä et al., 2010), where the values of storage and loss modulus were calculated from the loading curve using Dynamic Mechanical

Journal of Biomechanics, Volume 49, Issue 14, Issue October, 2016, Pages 3444-3451
DOI: 0.1016/j.jbiomech.2016.09.016

Analysis (CSM V3.75), using stabalised data after a penetration depth over 100nm.

Statistical Analysis

The mean and the standard deviation were reported for all the morphometric, mechanical and nanoindentation parameters. Comparisons were made between *mdx* and each of the other three genotypes, Wild-type (WT), P2X7$^{-/-}$ and *mdx*/P2X7$^{-/-}$. The non-parametric Kruskal-Wallis test was used to test the difference between each pair (i.e. WT vs *mdx*; P2X7$^{-/-}$ vs *mdx* and *mdx*/P2X7$^{-/-}$ vs *mdx*) and significant differences were indicated when p-value<0.05. All test assumptions were verified and analyses were carried out using SPSS (PASW version 18.0).

RESULTS

Morphometric analysis

The morphometric properties of the four genotypes in both cortical (midtibia) and trabecular (proximal tibial metaphyseal) bones are presented in Table 2, and comparisons were made between the results of *mdx* and each of the other three genotypes. In cortical bones, the *mdx*/P2X7$^{-/-}$ mice have significantly lower total cross-sectional area (Tt.Ar) than those of all the other three types (WT (p=0.004); P2X7$^{-/-}$ (p=0.004) and mdx (p=0.004), consistently, the SMA in *mdx*/P2X7$^{-/-}$ mice is significantly lower than all the other three types, suggesting smaller bones in the double knockout mice. By contrast, however, the cortical bone area (Ct.Ar) and cortical area fraction (Ct.Ar/Tt.Ar) of *mdx*/P2X7$^{-/-}$ mice are significantly higher than those of *mdx*. For trabecular bones, significantly higher BV/TV of *mdx*/P2X7$^{-/-}$ mice is also found compared with that of *mdx*, although the other parameters, including trabecular thickness, spacing and connectivity, are not statistically different between those of *mdx*/P2X7$^{-/-}$ and mdx mice. These results clearly show a positive impact of P2RX7 ablation on both cortical bone and trabecular bone.

Mechanical Properties

Figure 2 shows the individual stress-strain curves for the four genotypes, from which stiffness, maximum load, work-to-fracture, strain at failure were determined, whilst the flexural strength was calculated using Eq. (1). Post-yield stress-strain curves clearly show greater strain to failure in mdx/P2X7$^{-/-}$ bones than most of the other types including those of mdx. Table 3 shows the mean and the standard deviation of the mechanical properties for the four genotypes, and statistically significant differences are indicated. Significantly lower stiffness (by 53%, p=0.010) is found in *mdx*/P2X7$^{-/-}$ compared to that of *mdx*. Although the average maximum load achieved in *mdx*/P2X7$^{-/-}$ bones is relatively lower than that of mdx bones (2.43$\pm$0.45 vs 3.10$\pm$0.90), the average flexural strength in *mdx*/P2X7$^{-/-}$ bones is relatively higher than that of *mdx* bones (62.97$\pm$17.39 vs 49.65$\pm$19.09. Figure 3 shows the measured mean, the standard deviation and the spread of the mechanical properties, including the medians, the 25 and 75 percentiles and the outliers, in boxplots for the four genotypes. It seems that the measured low maximum load and stiffness in the *mdx*/P2X7$^{-/-}$ bones have not translated into low material properties. In fact relatively higher, although not statistically significant, average flexural strength and work-to-fracture are found in the *mdx*/P2X7$^{-/-}$ mice compared with those of *mdx* (Table 2). Significantly higher strain at failure is obtained in the *mdx*/P2X7$^{-/-}$ mice compared with those of both WT (by 60%, p=0.008) and *mdx* mice (by 79%, p=0.008), indicating greater ductility and resistance to fracture.

The fracture surfaces of the typical samples are shown in Figure 4. More brittle type of fracture found in *mdx* mice stands in contrast to the more ductile fracture found in the *mdx*/P2X7$^{-/-}$ bones as well as in the WT. The paths of the fracture are indicated in Figure 4(A), where instantaneous brittle fracture along the weak planes appears to be found in *mdx* bone, as opposed to the fibrous fracture surfaces found in WT and the knock-out bones, latter indicating gradual separation of the bones as a result of competition between cracking and fibre bridging. Figure 4(B) shows the cross sections of the failed samples, where the posterior surface was in tension and anterior surface was in compression. High magnification images at selected resolutions are shown in Figure 4(C) to reveal the micro-fracture mechanisms in the posterior area, where maximum tension led to the initiation of cracks. It seems that rougher fracture surfaces characterise the samples of WT, P2X7$^{-/-}$ and *mdx*/P2X7$^{-/-}$, as opposed to relatively smoother fracture surfaces in *mdx* bones. This observation seems to be consistent with the results presented in Table 3 and Figure 3, where higher values of strain at failure and work-to-fracture are obtained from the *mdx*/P2X7$^{-/-}$ bones compared with those from the *mdx* bones.

Nanoindentation

Table 4 shows the mean and the standard deviation of nano-indentation parameters from the advanced (Table 4a) and the dynamic (Table 4b) protocols. For

Journal of Biomechanics, Volume 49, Issue 14, Issue October, 2016, Pages 3444-3451
DOI: 0.1016/j.jbiomech.2016.09.016

cortical bones, statistically significant differences in the hardness, indentation modulus, elasticity and creep are observed between *mdx* and WT; and between *mdx*/P2X7$^{-/-}$ and *mdx* mice. Significantly lower hardness and elasticity (the elastic part of the indentation work), but higher creep and modulus are found in the *mdx* mice than in the WT mice; whilst lower modulus and creep but higher hardness and elasticity are found in the *mdx*/P2X7$^{-/-}$ than those in *mdx* mice, hence the double-mutant mice show properties closer to those of WT than those of *mdx*. For trabecular bones, however, there seem no statistically significant differences between the properties of WT and *mdx*; and those of *mdx*/P2X7$^{-/-}$ and *mdx*. Similar values in elasticity and creep are obtained across the genotypes, although significant differences are found in hardness and modulus between the knockout and WT bones.

For dynamic indentation, the elasticity in the cortical bones of *mdx* mice is significantly lower than that of WT mice ($p=0.007$), whilst higher storage modulus is found in *mdx* trabecular bones than that in WT mice ($p=0.001$). Statistically significant difference is found in loss modulus ($p=0.025$) between the *mdx*/P2X7$^{-/-}$ and the *mdx* in the cortical bone. Otherwise the values of storage modulus (trabecular bone), loss modulus (trabecular bone) and elasticity (cortical bone) in the *mdx*/P2X7$^{-/-}$ bones appear to be closer to those of WT mice.

A linear regression analysis shows that creep decreases with the increase in elasticity for all WT, *mdx* and *mdx*/P2X7$^{-/-}$ bones ($p<0.01$), and the negative correlations between creep and elasticity are shown in Figure 5 for cortical bones.

DISCUSSION

In this work, the effects of P2RX7 ablation on bone morphological, mechanical and tissue parameters have been examined. As revealed from the Kruskal-Wallis analysis, the ablation led to smaller bones, with significantly lower cross-sectional area (Tt.Ar) and SMA in *mdx*/P2X7-/- mice than other types. However, significantly more bone per area/per volume is found in *mdx*/P2X7-/- mice than all other types, as indicated by the significantly higher bone area (Ct.Ar) and bone area ratio (Ct.Ar/Tt.Ar) for cortical bone, and significantly higher bone volume fraction (BV/TV) for trabecular bone. The ablation does not seem to affect the architecture of the trabecular bone though, as indicated by the similar values of trabecular thickness (Tb.Th), trabecular spacing (Tb.Sp) and connectivity (Conn.D), as shown in Table 2. Compared with *mdx* bones, *mdx*/P2X7-/- mice have significantly higher cortical bone area (0.172 ± 0.01 vs 0.130 ± 0.018, mm^2), significantly higher cortical bone area ratio (0.411 ± 0.031 vs 0.360 ± 0.015, %) and significantly higher trabecular bone volume fraction (0.18 ± 0.036 vs 0.125 ± 0.027, % Table 2), higher average flexural strength (62.97 ± 17.39 vs 49.65 ± 19.09, MPa), work to fracture (4.59 ± 2.06 vs 3.31 ± 1.36, Nmm) and significantly higher strain at fracture (0.39 ± 0.12 vs 0.14 ± 0.04)(Table 3). In terms of tissue properties, hardness and elasticity are significantly higher whilst indentation modulus and creep significantly lower than those of *mdx*. Thus overall the ablation seems to have improved the bone properties. Preliminary work (n=2) has also been carried out to measure the bone mass using Thermogravimetry Analysis (TGA), where both mineral and organic contents are slightly higher in *mdx*/P2X7$^{-/-}$ bones than those in *mdx* bones (10.82 ± 1.17 vs 9.53 ± 0.43; 25.79 ± 1.52 vs 21.06 ± 0.24), which might have contributed to the higher flexural strength and strain to failure.

The mechanisms that led to the changes in the bones due to the loss of P2RX7 may be complex and require further studies, which are beyond the scope of this paper. It is known, however, that P2RX7 is expressed in both osteoblasts and osteoclasts, but it appears to have significantly different roles in bone physiology and in disease states. It is unclear if P2RX7 knockout affects bone formation or bone resorption or, perhaps, both (Agrawal and Gartland, 2015; Ke et al., 2003). In this work, we have examined the influence of P2RX7 inhibition, which is known to have therapeutic effects on skeletal muscles, on the morphological and the mechanical behaviour of the bones. Given that the bone abnormalities in mdx mice have been linked to chronic inflammation (Abou-Khalil et al., 2014), the reduced inflammation found in *mdx*/P2X7-/- muscles (Sinadinos et al., 2015) may be responsible for the reduced bone loss in these mice. Importantly, the significantly higher bone volume in both cortical and trabecular *mdx*/P2X7-/- bones would seem to suggest that the *overall* effect of the ablation is bone formation for the models we studied. The longer-term effects of P2RX7 receptor ablation have also been tested, and there is a significant improvement in bones of 6 months old mdx/P2RX7-/- mice (Sinadinos et al., 2015). However, at this stage it is difficult to ascertain whether the mechanism is not secondary to the improvements in muscle morphology observed in the later phases of mdx pathology.

Quantitative assessments of strength and toughness of small animal bones may be carried out using a number of approaches (Jepsen et al., 2015; Ritchie et al., 2008). For toughness characterisation, work-to-fracture has the advantage of measuring both strength and toughness using the same un-notched specimen at the same time, although the measured properties are usually size-dependent. Fracture toughness measurements require a pre-crack, which is considered best suited for characterisation of the inherent resistance of a material to fracture (Ritchie et al., 2008). In this work, we have adopted the former due to the similar sizes of the samples across the phenotypes, and for the convenience and the lack of ambiguity of the measured mechanical properties in strength, stiffness and work-to-fracture. Our approach follows the guidelines for the assessment of mechanical properties of mouse bones (Jepsen et al., 2015). A variety of toughening mechanisms (Li et al., 2013) might be at work giving rise to the ductile behaviour observed particularly in *mdx*/P2X7$^{-/-}$ bones. Pulling out of collagen fibrils can be observed particularly in P2X7$^{-/-}$ and *mdx*/P2X7$^{-/-}$, where twisted collagen fibrils are also evident. This may interrupt the propagation of cracks resulting in higher resistance to fracture and greater strain to failure.

In this work the specimens were fixed in phosphate buffered formal saline (PBFS) solution for long term storage with limited tissue shrinkage for CT scanning and mechanical testing. Although fixing bone samples in formalin is one of the common fixation methods for microscopic studies, there have been reports on the variation of the strength measured in embalmed samples, possibly due to increase in collagen cross-linking. Nevertheless, as the same fixation method was used for all the samples examined here, the relative values of mechanical properties obtained should be useful for comparison purposes. The nanoindentation was carried out in dry conditions, a common practice adopted for easy comparison with published work and for reducing some of the influential factors such as vibration noise and hydration state of the bones. Although the modulus measured in wet is known to be about 10-20% lower than that in dry, this was not considered an issue for group comparison purposes.

CONCLUDING REMARKS

P2RX7 ablation has produced some significant improvements in the morphometric, mechanical and tissue properties of dystrophic long bones. Our results show that the curative impact of this receptor ablation on the bone pathology is notable from the very early phase of disease. This effect seems long-lasting as we have found improved morphometric bone parameters in 6 month old *mdx*/P2X7$^{-/-}$ mice (Sinadinos et al., 2015), although the life-long effects of P2RX7 ablation on such properties remain to be studied. Nevertheless the current results seem to be encouraging in that selective P2RX7 antagonists might be of promise as a candidate for therapeutic trials for the treatment of this lethal disease.

Acknowledgements

NSM is funded by postgraduate scholarship from Malaysia Government. . This work was also supported, in parts, by grants from the Duchenne Parents Project NL (https://www.duchenne.nl/) and the EU Interreg IV (TC2N; http://www.interreg4a-2mers.eu/en). We thank Mr C Lupton and Dr G Tozzi for their assistance in the µCT imaging and the mechanical testing; Professor Simon Cragg for the SEM work and Professor Matt Guille for helpful discussion.

Conflict of Interest

All authors declare no conflict of interests.

References

Abou-Khalil, R., Yang, F., Mortreux, M., Lieu, S., Yu, Y.Y., Wurmser, M., Pereira, C., Relaix, F., Miclau, T., Marcucio, R.S., Colnot, C., 2013. Delayed bone regeneration is linked to chronic inflammation in murine muscular dystrophy. J. Bone Miner. Res. 29, 304–315. doi:10.1002/jbmr.2038

Agrawal, A., Gartland, A., 2015. P2X7 receptors: role in bone cell formation and function. J. Mol. Endocrinol. 54, R75–R88. doi:10.1530/JME-14-0226

Anderson, J.E., Lentz, D.L., Johnson, R.B., 1993. Recovery from disuse osteopenia coincident to restoration of muscle strength in mdx mice. Bone 14, 625–634.

Bianchi, M.L., Mazzanti, A., Galbiati, E., Saraifoger, S., Dubini, A., Cornelio, F., Morandi, L., 2003. Bone mineral density and bone metabolism in Duchenne muscular dystrophy. Osteoporos. Int. 14, 761–7. doi:10.1007/s00198-003-1443-y

Bianchi, M.L., Morandi, L., 2008. Duchenne Muscular Dystrophy Evaluating Bone and Mineral Metabolism in Patients with Duchenne Muscular Dystrophy. Eur. Musculoskelet. Rev. 80–83.

Journal of Biomechanics, Volume 49, Issue 14, Issue October, 2016, Pages 3444-3451
DOI: 0.1016/j.jbiomech.2016.09.016

Blake, D.J., Weir, A., Newey, S.E., Davies, K.E., 2002. Function and genetics of dystrophin and dystrophin-related proteins in muscle. Physiol. Rev. 82, 291–329. doi:10.1152/physrev.00028.2001

Bouxsein, M.L., Boyd, S.K., Christiansen, B. a, Guldberg, R.E., Jepsen, K.J., Müller, R., 2010. Guidelines for assessment of bone microstructure in rodents using micro-computed tomography. J. Bone Miner. Res. 25, 1468–86. doi:10.1002/jbmr.141

Bozzola, J.J., Russel, L.D., 1999. Electron Microscopy: Principles and Techniques for Biologist. Jones and Bartlett Publishers.

Bulfield, G., Siller, W.G., Wight, P. a, Moore, K.J., 1984. X chromosome-linked muscular dystrophy (mdx) in the mouse. Proc. Natl. Acad. Sci. U. S. A. 81, 1189–1192. doi:10.1073/pnas.81.4.1189

Doube, M., Kłosowski, M.M., Arganda-carreras, I., Fabrice, P., 2010. BoneJ : free and extensible bone image analysis in ImageJ. Bone 47, 1076–1079. doi:10.1016/j.bone.2010.08.023.BoneJ

Ferrari, D., Munerati, M., Melchiorri, L., Hanau, S., di Virgilio, F., Baricordi, O.R., 1994. Responses to extracellular ATP of lymphoblastoid cell lines from Duchenne muscular dystrophy patients. Am. J. Physiol. 267, C886–C892.

Finnilä, M.A.J., Zioupos, P., Herlin, M., Miettinen, H.M., Simanainen, U., Håkansson, H., Tuukkanen, J., Viluksela, M., Jämsä, T., 2010. Effects of 2,3,7,8-tetrachlorodibenzo-p-dioxin exposure on bone material properties. J. Biomech. 43, 1097–103. doi:10.1016/j.jbiomech.2009.12.011

Gartland, A., 2012. P2X receptors in bone. Wiley Interdiscip. Rev. Membr. Transp. Signal. 1, 221–227. doi:10.1002/wmts.26

Herlin, M., Finnilä, M. a J., Zioupos, P., Aula, A., Risteli, J., Miettinen, H.M., Jämsä, T., Tuukkanen, J., Korkalainen, M., Håkansson, H., Viluksela, M., 2013. New insights to the role of aryl hydrocarbon receptor in bone phenotype and in dioxin-induced modulation of bone microarchitecture and material properties. Toxicol. Appl. Pharmacol. 273, 219–26. doi:10.1016/j.taap.2013.09.002

ISO4577-1:2015, Metallic materials -Instrumented indentation test for hardness and materials parameters - Part 1: Test method.

Jepsen, K.J., Silva, M.J., Vashishth, D., Guo, X.E., van der Meulen, M.C.H., 2015. Establishing Biomechanical Mechanisms in Mouse Models: Practical Guidelines for Systematically Evaluating Phenotypic Changes in the Diaphyses of Long Bones. J. Bone Miner. Res. n/a–n/a. doi:10.1002/jbmr.2539

Ke, H.Z., Qi, H., Weidema, a F., Zhang, Q., Panupinthu, N., Crawford, D.T., Grasser, W. a, Paralkar, V.M., Li, M., Audoly, L.P., Gabel, C. a, Jee, W.S.S., Dixon, S.J., Sims, S.M., Thompson, D.D., 2003. Deletion of the P2X7 nucleotide receptor reveals its regulatory roles in bone formation and resorption. Mol. Endocrinol. 17, 1356–67. doi:10.1210/me.2003-0021

Li, S., Abdel-Wahab, A., Silberschmidt, V. V., 2013. Analysis of fracture processes in cortical bone tissue. Eng. Fract. Mech. 110, 448–458. doi:10.1016/j.engfracmech.2012.11.020

Nakagaki, W.R., Bertran, C.A., Matsumura, C.Y., Santo-Neto, H., Camilli, J.A., 2011. Mechanical, biochemical and morphometric alterations in the femur of mdx mice. Bone 48, 372–379. doi:10.1016/j.bone.2010.09.011

Nakagaki, W.R., Camilli, J.A., 2012. Bone tissue and muscle dystrophin deficiency in mdx mice. Joint. Bone. Spine 79, 129–33. doi:10.1016/j.jbspin.2011.08.004

Novotny, S.A., Warren, G.L., Lin, A.S., Gulderg, R.E., Kristen, A., Lowe, D.A., 2011. Bone is functionally impaired in dystrophic mice but less so than skeletal muscle. Neuromuscul. Disord. 21, 612–625. doi:10.1016/j.nmd.2010.12.002.Bone

Oliver, W.C., Pharr, G.M., 1992. An improved technique for determining hardness and elastic modulus using load and displacement sensing indentation experiments. Mater. Res. 7, 1564–1583.

Ridler, T.W., Calvard, S., 1978. Picture Thresholding Using an Iterative Selection Method. IEEE Trans. Syst. Man , Cybernatics 630–632.

Ritchie, R.O., Koester, K.J., Ionova, S., Yao, W., Lane, N.E., Ager, J.W., 2008. Measurement of the toughness of bone: a tutorial with special reference to small animal studies. Bone 43, 798–812. doi:10.1016/j.bone.2008.04.027

Rufo, A., Del Fattore, A., Capulli, M., Carvello, F., De Pasquale, L., Ferrari, S., Pierroz, D., Morandi, L., De Simone, M., Rucci, N., Bertini, E., Bianchi, M.L., De Benedetti, F., Teti, A., 2011. Mechanisms inducing low bone density in Duchenne muscular dystrophy in mice and humans. J. Bone Miner. Res. 26, 1891–903. doi:10.1002/jbmr.410

Saito, M., Marumo, K., 2010. Collagen cross-links as a determinant of bone quality: a possible explanation for bone fragility in aging, osteoporosis, and diabetes mellitus. Int. Osteoporos. 21, 195–214. doi:10.1007/s00198-009-1066-z

Silva, M.J., Brodt, M.D., Fan, Z., Rho, J.-Y., 2004. Nanoindentation and whole-bone bending estimates of material properties in bones from the senescence accelerated mouse SAMP6. J. Biomech. 37, 1639–46. doi:10.1016/j.jbiomech.2004.02.018

Sinadinos, A., Young, C., Al-Khalidi, R., Teti, A., Kalinski, P., Mohamad, S., Floriot, L., Henry, T., Tozzi, G., Jiang, T., Wurtz, O., Lefebvre, A., Tong, J., Vaudry, D., Arkle, S., DoRego, J.-C., Gorecki, D., Shugay, M., 2015. P2RX7 Purinoceptor: A Therapeutic Target for Ameliorating the Symptoms of Duchenne Muscular Dystrophy. PLoS Med 12(10), 1–33. doi:10.1371/journal.pmed.1001888

Söderpalm, A.-C., Magnusson, P., Ahlander, A.-C., Karlsson, J., Kroksmark, A.-K., Tulinius, M., Swolin-Eide, D., 2007. Low bone mineral density and decreased bone turnover in Duchenne muscular dystrophy. Neuromuscul. Disord. 17, 919–28. doi:10.1016/j.nmd.2007.05.008

Solle, M., Labasi, J., Perregaux, D.G., Stam, E., Petrushova, N., Koller, B.H., Griffiths, R.J., Gabel, C. a., 2001. Altered cytokine production in mice lacking P2X7 receptors. J. Biol. Chem. 276, 125–132. doi:10.1074/jbc.M006781200

Stock, S.R., 2009. MicroComputed Tomography: methodology and applications. Taylor & Francis Group, United States of America.

Turner, C.H., 2002. Determinants of skeletal fragility and bone quality. J. Musculoskelet. Neuronal Interact. 2, 527–8.

Vashishth, D., 2008. Small Animal Bone Mechanics. Bone 43, 794–797. doi:10.1016/j.bone.2008.06.013.Small

Yeung, D., Zablocki, K., Lien, C.-F., Jiang, T., Arkle, S., Brutkowski, W., Brown, J., Lochmuller, H., Simon, J., Barnard, E. a, Górecki, D.C., 2006. Increased susceptibility to ATP via alteration of P2X receptor function in dystrophic mdx mouse muscle cells. FASEB J. 20, 610–620. doi:10.1096/fj.05-4022com

Young, C.N., Sinadinos, A., Lefebvre, A., Chan, P., Arkle, S., Vaudry, D., Gorecki, D.C., 2015. A novel mechanism of autophagic cell death in dystrophic muscle regulated by P2RX7 receptor large-pore formation and HSP90. Autophagy 11, 113–130. doi:10.4161/15548627.2014.994402

Young, C.N.J., Brutkowski, W., Lien, C.-F., Arkle, S., Lochmüller, H., Zabłocki, K., Górecki, D.C., 2012. P2X7 purinoceptor alterations in dystrophic mdx mouse muscles: relationship to pathology and potential target for treatment. J. Cell. Mol. Med. 16, 1026–37. doi:10.1111/j.1582-4934.2011.01397.x

Zhang, R., Gong, H., Zhu, D., Ma, R., Fang, J., Fan, Y., 2015. Multi-level femoral morphology and mechanical properties of rats of different ages. Bone 76, 76–87. doi:10.1016/j.bone.2015.03.022

Zioupos, P., Rogers, K.D., 2006. Complementary Physical and Mechanical Techniques to Characterise Tooth: A Bone-like Tissue. J. Bionic Eng. 3, 19–31. doi:10.1016/S1672-6529(06)60003-6

Journal of Biomechanics, Volume 49, Issue 14, Issue October, 2016, Pages 3444-3451
DOI: 0.1016/j.jbiomech.2016.09.016

Table 1. The types of mouse used in this study.

Genotype	Genetic background	Age	Gender	n
WT	C57BL10, wild-type mice.	28 days	Male	6
mdx	DMD gene mutant (dystrophic) mice on the C57BL10 background (Bulfield et al., 1984).	29 days and 31 days	Male	6
P2RX7$^{-/-}$	P2RX7 receptor knockout mice (Solle et al., 2001).	29 days and 31 days	Male	6
mdx/P2RX7$^{-/-}$	*mdx* and P2RX7 receptor knockout (double mutant) mice (Young et al., 2015).	28 days	Male	6

Table 2. Morphometric properties of the bones of the genotypes studied.

Properties	**WT**	***mdx***	**P2RX7$^{-/-}$**	**mdx/P2RX7$^{-/-}$**
Cortical				
(Midtibia)				
Tt.Ar (mm^2)	1.344±0.263	1.216±0.114	1.089±0.139	**0.722±0.123** [a,b,c]
Ct.Ar (mm^2)	0.160±0.017	**0.130±0.018**[a]	**0.161±0.030**[b]	**0.172±0.01**[b]
Ct.Ar/Tt.Ar (%)	0.405±0.038	0.360±0.015	0.419±0.026	**0.411±0.031**[a,b,c]
Cr.Th (mm)	0.150±0.017	**0.123±0.010**[a]	0.137±0.014	**0.115±0.009**[a,c]
Second Moment of Area (SMA) (mm^4)	0.11±0.03	0.09±0.03	0.08±0.03	**0.04±0.01**[a,b,c]
Trabecular				
(Proximal tibial metaphyseal)				
BV/TV (%)	0.193±0.066	**0.125±0.027**[a]	**0.265±0.125**[b]	**0.180±0.036**[b]
Trab.Th (mm)	0.052±0.004	**0.042±0.004**[a]	0.053±0.015	**0.043±0.005**[a]
Trab.Sp (mm)	0.258±0.055	0.242±0.040	**0.190±0.028**[a,b]	0.223±0.059
Conn.D (1/mm^3)	113.92±73.05	162.41±90.16	140.79±76.86	125.98±93.19

[a,b,c] and **bold text** indicate p<0.05 (Kruskal-Wallis)
[a]statistically significant difference (<0.05) with WT.
[b]statistically significant difference (<0.05) with *mdx*.
[c]statistically significant difference (<0.05) with P2RX7$^{-/-}$.

Journal of Biomechanics, Volume 49, Issue 14, Issue October, 2016, Pages 3444-3451
DOI: 0.1016/j.jbiomech.2016.09.016

Table 3. The mechanical properties of the bones of the genotypes.

Bone properties	**WT**	***mdx***	**P2RX7$^{-/-}$**	***mdx*/P2RX7$^{-/-}$**
Maximum load (N)	4.99±0.89	**3.10±0.90[a]**	4.32±1.63	**2.43±0.45[a,c]**
Stiffness (N/mm)	12.16±2.12	**7.19±2.58[a]**	**8.64±2.73[a]**	**3.38±1.51[a,b,c]**
Work-to-fracture (N·mm)	4.01±1.00	3.31±1.36	5.79±2.02	4.59±2.06
Flexural Strength (MPa)	60.49±9.74	49.65±19.09	73.36±48.27	62.97±17.39
Strain at Failure	**0.15±0.02[c]**	0.14±0.04	**0.37±0.15[b]**	**0.39±0.12[a,b]**

[a,b,c] and **bold text** indicate p<0.05 (Kruskal-Wallis)
[a]statistically significant difference (<0.05) with WT.
[b] statistically significant difference (<0.05) with *mdx*.
[c] statistically significant difference (<0.05) with P2RX7$^{-/-}$.

Table 4a. Nanoindentation results produced by using the 'advanced' loading protocol for the tissue properties of the mouse bones.

Material properties	**WT**	***mdx***	**P2RX7$^{-/-}$**	**mdx/P2RX7$^{-/-}$**
Cortical Advanced				
Hardness (MPa)	643.65±66.62	**616.27±57.42[a]**	628.36±57.36	**637.89±49.58[b]**
Ind. Modulus (GPa)	17.28±1.91	**18.31±1.52[a]**	**16.87±1.22[b]**	**17.44±1.28[b,c]**
Elasticity (%)	22.88±2.25	**20.34±2.12[a]**	**22.76±2.75[b]**	**22.63±2.59[b]**
Creep (%)	5.89±1.05	**6.81±1.15[a]**	**6.02±1.23[b]**	**5.92±0.91[b]**
Trabecular Advanced				
Hardness (MPa)	437.14±104.63	475.65±97.37	**523.46±98.60[a]**	**505.79±102.47[a]**
Ind. Modulus (GPa)	10.97±1.87	11.77±2.18	**12.56±1.98[a]**	**12.48±2.07[a]**
Elasticity (%)	24.58±2.86	24.40±3.56	24.93±4.80	24.40±3.60
Creep (%)	6.53±1.08	6.77±1.90	6.18±2.17	6.55±1.58

[a,b,c] and **bold text** indicate p<0.05 (Kruskal-Wallis)
[a]statistically significant difference (<0.05) with WT.
[b]statistically significant difference (<0.05) with *mdx*.
[c]statistically significant difference (<0.05) with P2RX7$^{-/-}$.

Journal of Biomechanics, Volume 49, Issue 14, Issue October, 2016, Pages 3444-3451
DOI: 0.1016/j.jbiomech.2016.09.016

Table 4b. Nanoindentation results produced by using the 'dynamic' loading protocol for the tissue properties of the mouse bones.

Material properties	**WT**	***mdx***	**P2RX7$^{-/-}$**	**mdx/P2RX7$^{-/-}$**
Cortical Dynamic				
Phase Difference (ð)	3.50±0.61	3.72±1.01	4.14±1.04	**4.13±0.91**[a]
Storage Modulus (GPa)	20.63±2.29	20.13±2.05	19.33±2.19	**21.31±1.86**[c]
Loss Modulus (GPa)	1.28±0.27	1.32±0.32	1.43±0.44	**1.56±0.33**[a,b]
Elasticity (%)	21.36±2.04	**19.36±1.78**[a]	**20.85±2.08**[b]	20.56±2.29
Trabecular Dynamic				
Phase Difference (ð)	4.75±1.58	4.95±2.42	4.08±1.67	4.23±1.18
Storage Modulus (GPa)	13.61±2.47	**16.92±2.74**[a]	**17.43±2.08**[a]	**15.45±2.42**[a,c]
Loss Modulus (GPa)	1.07±0.46	1.50±0.74	1.24±0.45	1.17±0.41
Elasticity (%)	23.10±3.01	22.53±3.22	24.25±5.09	21.62±3.27

[a,b,c] and **bold text** indicate $p<0.05$ (Kruskal-Wallis)
[a]statistically significant difference (<0.05) with WT.
[b]statistically significant difference (<0.05) with *mdx*.
[c]statistically significant difference (<0.05) with P2RX7$^{-/-}$.

Journal of Biomechanics, Volume 49, Issue 14, Issue October, 2016, Pages 3444-3451
DOI: 0.1016/j.jbiomech.2016.09.016

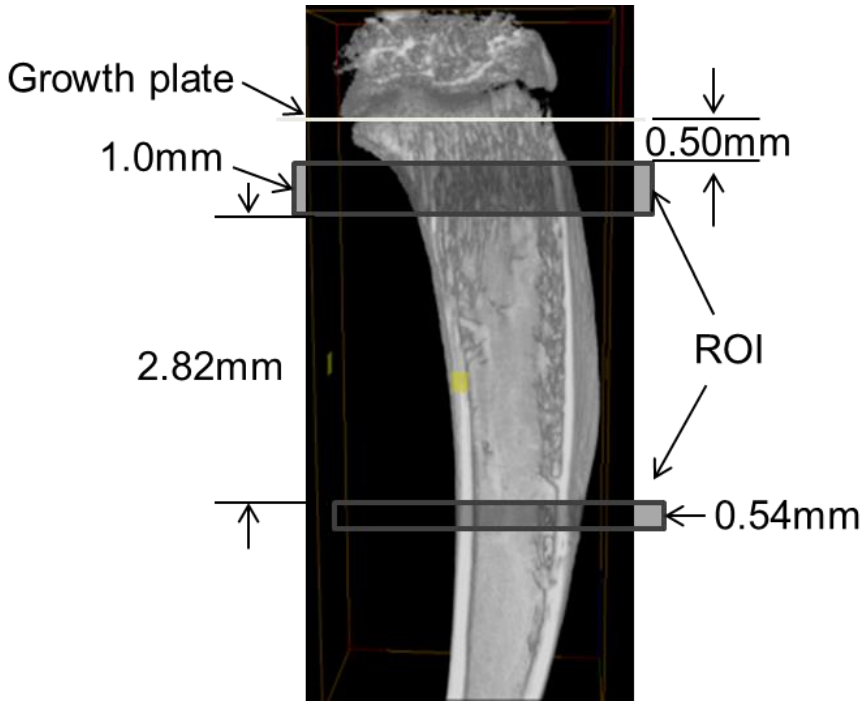

Figure 1. An illustration of the Regions of Interest (ROI) studied in this work at proximal tibia metaphyseal and mid-tibia.

Journal of Biomechanics, Volume 49, Issue 14, Issue October, 2016, Pages 3444-3451
DOI: 0.1016/j.jbiomech.2016.09.016

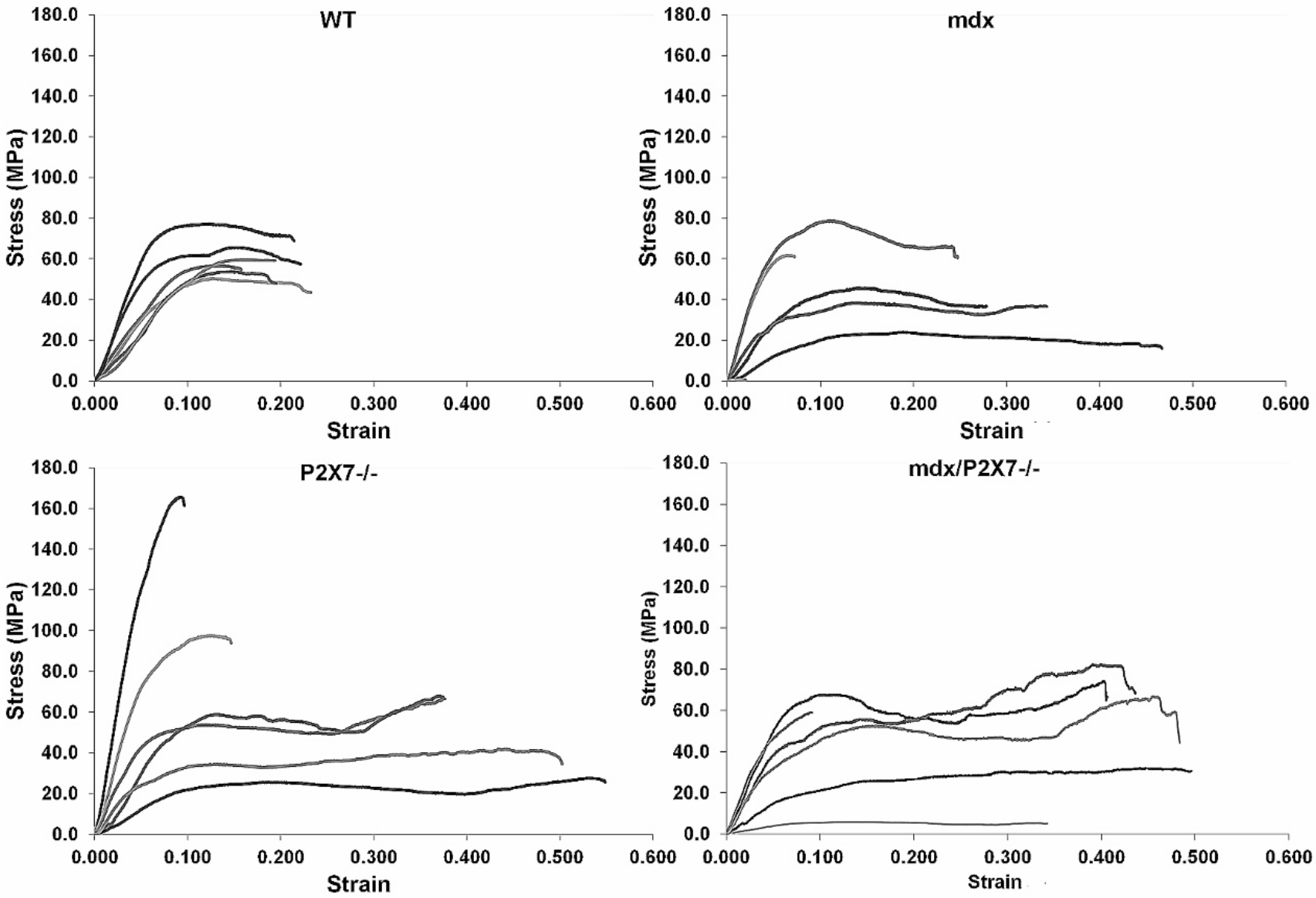

Figure 2. The stress-strain curves for the four genotypes (n=6).

Journal of Biomechanics, Volume 49, Issue 14, Issue October, 2016, Pages 3444-3451
DOI: 0.1016/j.jbiomech.2016.09.016

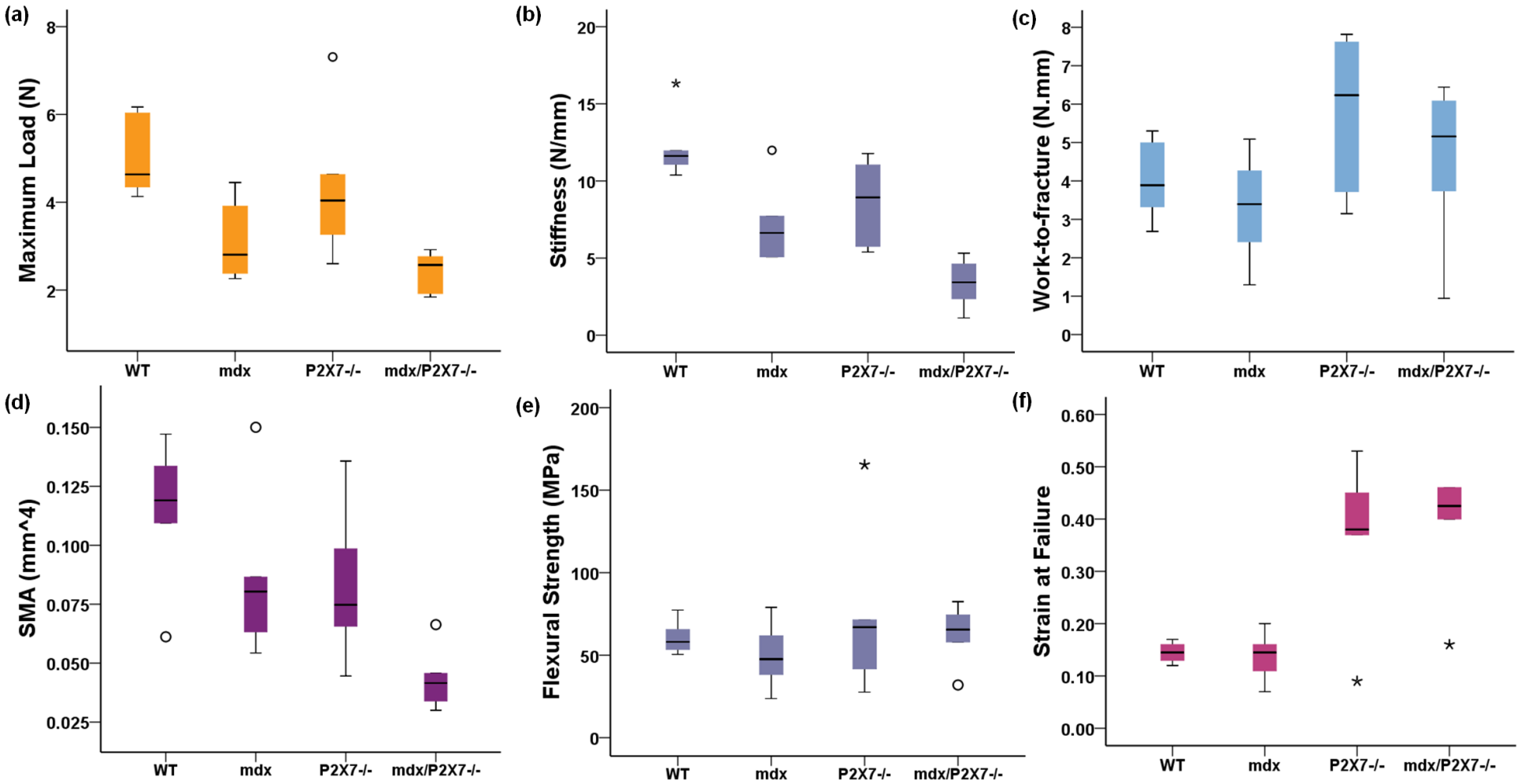

Figure 3. A comparison of the mechanical properties of bones obtained from the three-point-bending tests. (a) Maximum load; (b) flexural modulus; (c) work-to-fracture; (d) second moment of area (SMA); (e) flexural strength and (f) strain at failure. The boxplots for the four genotypes including the medians, the 25 and 75 percentiles and the outliers are also indicated.

Journal of Biomechanics, Volume 49, Issue 14, Issue October, 2016, Pages 3444-3451
DOI: 0.1016/j.jbiomech.2016.09.016

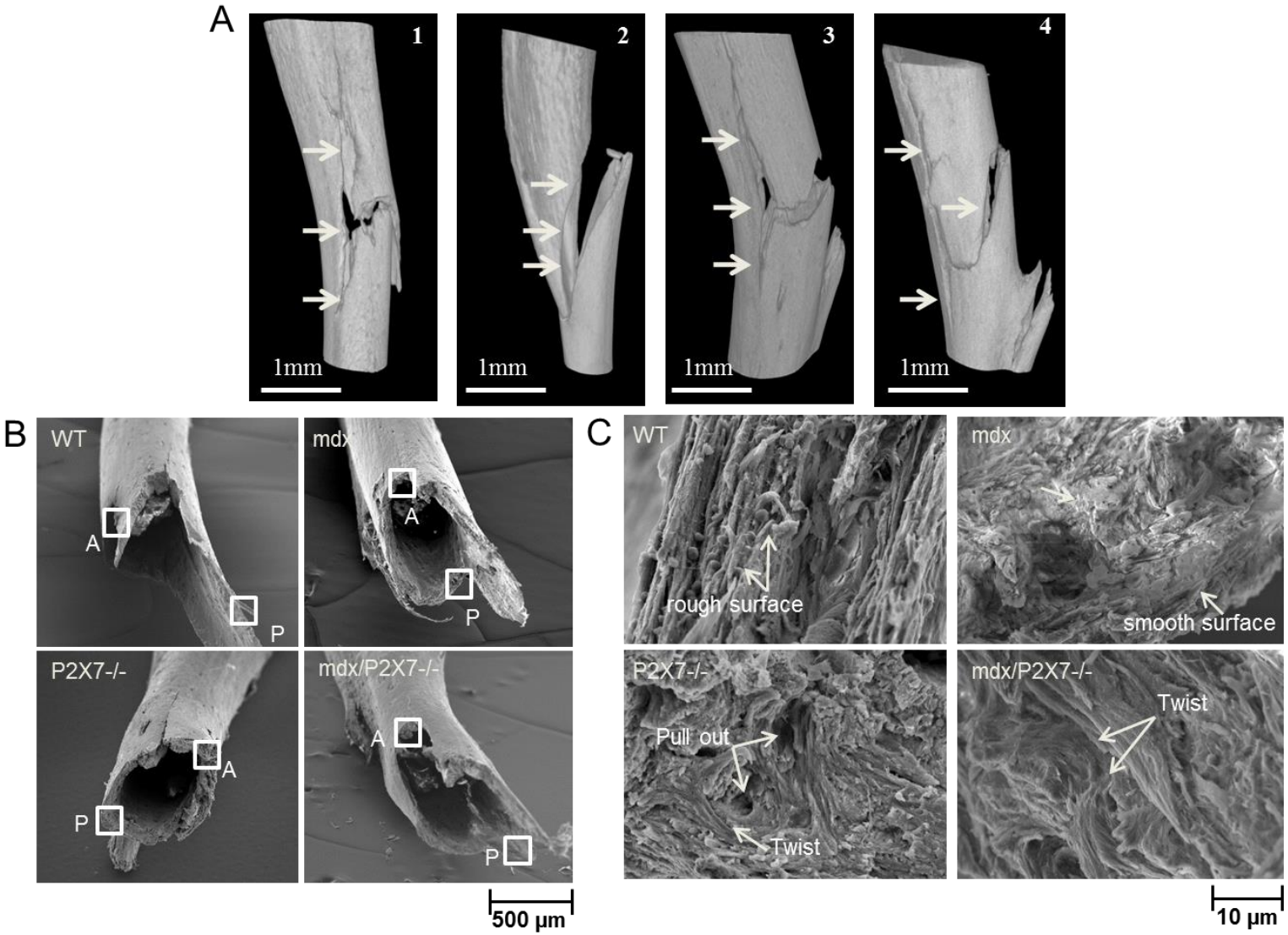

Figure 4. (A) The fracture morphologies of the genotypes post mechanical testing: 1) WT; 2) *mdx*; 3) P2RX7$^{-/-}$ and 4) *mdx*/P2RX7$^{-/-}$. The initiation of cracks path and subsequent fracture are indicated by the arrows. (B) The fracture surfaces of the samples post three-point-bending testing

Journal of Biomechanics, Volume 49, Issue 14, Issue October, 2016, Pages 3444-3451
DOI: 0.1016/j.jbiomech.2016.09.016

from the SEM analysis, where compression and tension were experienced in anterior (A) and posterior (P), respectively. (C) Details of the posterior cortex of the bones showing fibrous fracture surfaces in WT and double mutant bones, as opposed to brittle fracture surfaces in *mdx* bone.

Journal of Biomechanics, Volume 49, Issue 14, Issue October, 2016, Pages 3444-3451
DOI: 0.1016/j.jbiomech.2016.09.016

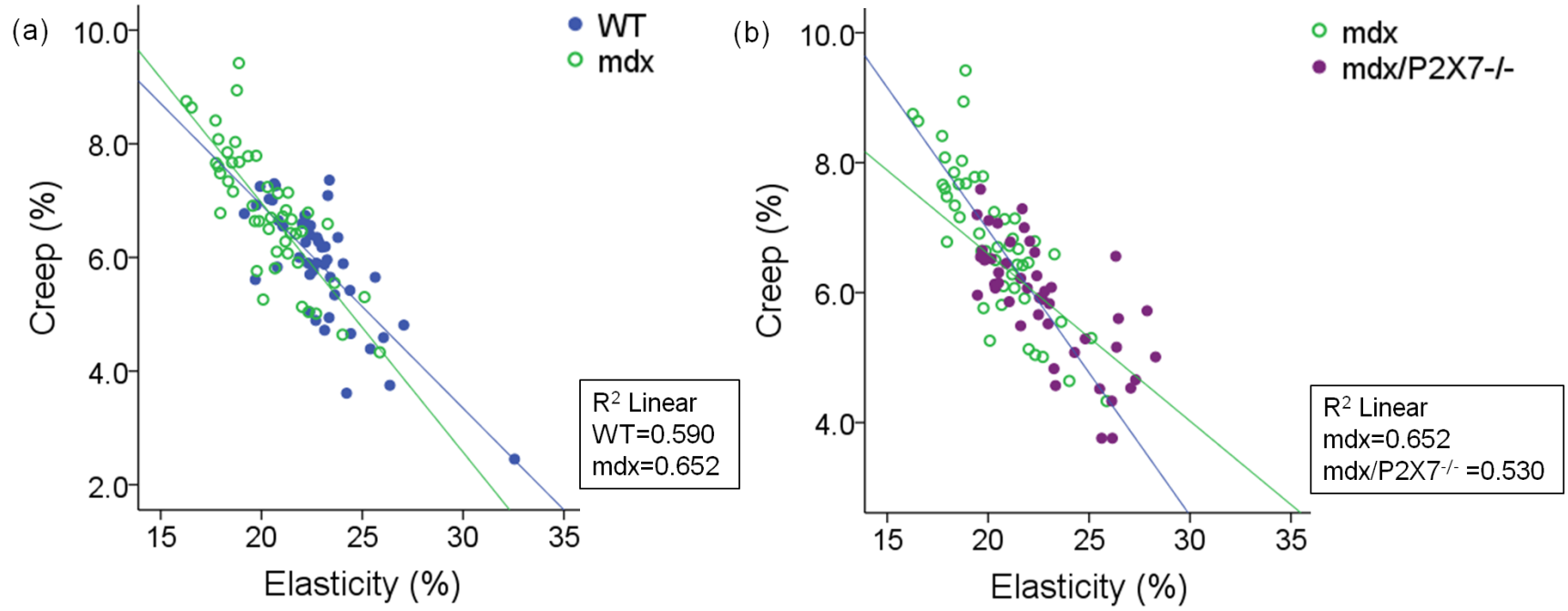

Figure 5. The correlation between creep and elasticity of the cortical bones of (a) WT and *mdx* and (b) *mdx* and *mdx*/P2X7$^{-/-}$ from the advanced nanoindentation. The results seem to suggest that P2RX7$^{-/-}$ ablation reverses, to a large extent, the effects of the dystrophic abnormality, thus the tissue response of *mdx*/P2X7$^{-/-}$ is close to that of WT bones.